Trans Indian Inst Met (2021) 74(6):1361–1371
https://doi.org/10.1007/s12666-021-02229-2

ORIGINAL ARTICLE

Microstructure Evolution and Texture Characteristics of Pure Nickel N6 During Cold Rolling Process

Xuan Sun[1] · Zhi Jia[1,2] · Jinjin Ji[1] · Yanjiang Wang[1] · Baolin Wei[1] · Lidan Yu[1]

Received: 21 October 2020 / Accepted: 23 February 2021 / Published online: 20 March 2021

Abstract A single-pass large-deformation rolling method was used to study the effect of cold rolling degree on the microstructure, microtextural evolution, and grain orientation during the cold rolling of pure nickel N6. The results show that the microstructure evolves from micro-bands to lamellar-bands with the increase of cold rolling reduction, and the fraction of coincidence site lattice boundaries always decreases. Starting from an initially low imposed strain (20% of the cold rolling reduction), the deformed microstructure is mainly composed of Goss, rotated Goss, P, and Brass orientations. When cold rolling reduction exceeds 50%, the shear textures appear and other textures remain but their intensities decrease. The strong shear stress on the surface of the rolled plate causes the normal cold-rolled texture dominated by $Cu\{112\} < 111 >$, $S\{123\} < 634 >$, $Brass\{011\} < 211 >$ to rotate around the transverse direction to form a shear texture composed of $shear4\{112\} < 110 >$ and $\{110\}\|RD$ fiber textures.

Keywords Pure nickel · Microstructure · Texture · Grain orientation · EBSD

✉ Zhi Jia
jiazhi@lut.edu.cn

[1] School of Material Science and Engineering, Lanzhou University of Technology, Lanzhou, Gansu Province, China

[2] State Key Laboratory of Advanced Processing and Recycling of Nonferrous Metals, Lanzhou University of Technology, No.287 langongping Road, Qilihe District, Lanzhou 730050, Gansu Province, People's Republic of China

1 Introduction

With high-temperature resistance, oxidation resistance, and corrosion resistance in concentrated alkali solution [1, 2], pure nickel N6 is widely used in alkalis, aerospace applications, nuclear power, and other industrial fields [3]. Most material properties are structurally dependent, but structural applications of pure metals are generally strongly restricted by insufficient mechanical properties, which exclude them from practical engineering applications [4, 5]. Plastic deformation is a technique that can be used to effectively refine grains and improve mechanical properties of polycrystalline metals and alloys [6–9]. Deformation processing of materials is typically accompanied with the evolution of a unique texture and microstructure. It is worth noting that microstructural development during deformation processing is important for controlling mechanical properties [10–12]. There are textures in many metal products, which affect various properties of the material, such as strength, formability, and corrosion resistance. Therefore, proper understanding of microstructure and texture is necessary.

Cold rolling (CR) is a plastic deformation method that can be used to produce sheets and strip products that have uniform microstructures and good mechanical performance. A number of research studies have been carried out to understand the deformation mechanisms and, consequently, the development of texture during rolling of face-centered cubic (fcc) metals and alloys. For fcc metals with middle- and high-level dislocation energy, the microstructure is characterized by a lamellar structure elongated along the rolling direction, and the texture mainly includes S, Brass (Bs), and copper, three orientations after traditional large-deformation rolling [13, 14]. Related studies have shown that rolling path, rolling speed,

and heat treatment parameters and other related factors will directly affect the textural configuration of the alloy and then affect the macroscopic properties of the alloy [15–18]. Although there are some studies on the large deformation of cold rolling and annealing behavior of pure nickel [14, 19, 20], the cold rolling with large deformation is completed by multiple passes with small deformation in these researches. Small amount of plastic strain is not enough to refine the grain of the material to a sufficiently small extent, which affects the effect of grain refinement. For example, when Chen et al. [14] studied the evolution of annealing twins during the recrystallization and grain growth of high-rolled pure nickel, the highly rolled deformation is completed by multiple passes with 5% thickness reduction in one pass. So far there is a lack of systematic studies related to the effects of cold rolling degree under large-deformation conditions on microstructure and texture evolution of pure nickel N6.

Pure nickel N6 is mostly used in industrial fields in the form of pipes, but its use as a structural material is restricted due to uneven microstructure and poor strength. At home and abroad, the production of nickel and nickel-based superalloy pipes uses hot extrusion to produce raw pipes and then undergoes multiple passes of cold rolling and annealing to produce finished straight pipes. Cold rolling and subsequent annealing treatment are the final thermo-mechanical treatment process before the special heat treatment of nickel and nickel-based alloy tubes. The cold rolling directly determines the microstructure and mechanical properties of the finished tube, thereby determining the performance of the tube. Therefore, this paper will focus on the microstructure characteristics of pure nickel N6 with different cold rolling degrees after cold rolling to provide guidance for the actual production process microstructure control.

2 Materials and Methods

2.1 Material Processing

The investigated material was commercially pure nickel N6 (99.6%) in the form of plates, with its chemical composition shown in Table 1. The pure nickel N6 plate was cut into 30 mm × 10 mm × 6 mm (length × width × thickness) rolled specimens by a wire electric discharge machine for further experiments. Prior to cold rolling, the pure nickel N6 samples were annealed under vacuum at 973 K for 4 h and cooled in air to room temperature to form a fully recrystallized structure (Fig. 1a) ensuring high susceptibility to plastic deformation. After that, the samples were cold rolled at each step at room temperature on a laboratory rolling mill to either 20, 50, 70, and 90%. And the rolling method is symmetrical rolling.

2.2 Characterization Methods

Microstructural and microtextural features of nickel plates in as-annealed and cold deformed conditions were evaluated using an FEI Nova NanoSEM 430 scanning electron microscope (SEM) equipped with an electron backscatter diffraction system (EBSD). Microstructural observations were performed on the rolling direction–transverse direction (RD-TD) surface of the samples. The RD-TD surfaces of the specimens were ground using sandpapers from 400# to 3000# and then polished using a 0.5 μm diamond solution. For EBSD analysis, samples were polished by electro-polishing in a solution of 90 mL C_2H_5OH and 10 mL $HClO_4$ at − 20 °C at a voltage of 50 V. The scanning step length of as-annealed and small deformation samples were set to 2 μm, and the scanning step lengths of the large-deformation samples were set to 0.5 μm. The EBSD data were analyzed by Channel 5 software. The evolution of crystallographic texture was analyzed by calculating the orientation distribution functions (ODFs).

3 Results

3.1 Microstructural Evolution

Figure 1 displays the inverse pole figures and grain boundaries map, as well as the distribution of misorientation angles and grain diameters of as-annealed pure nickel N6. It can be seen from Fig. 1a that uniformly distributed grains and plenty of twins are observed. The average grain size of as-annealed pure nickel N6 is 29.3 μm (Fig. 1b). In Fig. 1c, different types of grain boundaries are represented by different colors. The coincidence site lattice (CSL) boundaries of the annealed samples account for 61.53%, and fractions of Σ3, Σ9, and Σ27 are 51.1%, 5.3%, and

Table 1 Chemical composition of pure nickel N6 (wt%)

Ni + Co	Cu	Fe	Mn	C	Si	S	Al	Ti
99.6	0.064	0.11	0.05	0.047	0.018	0.045	0.046	0.018

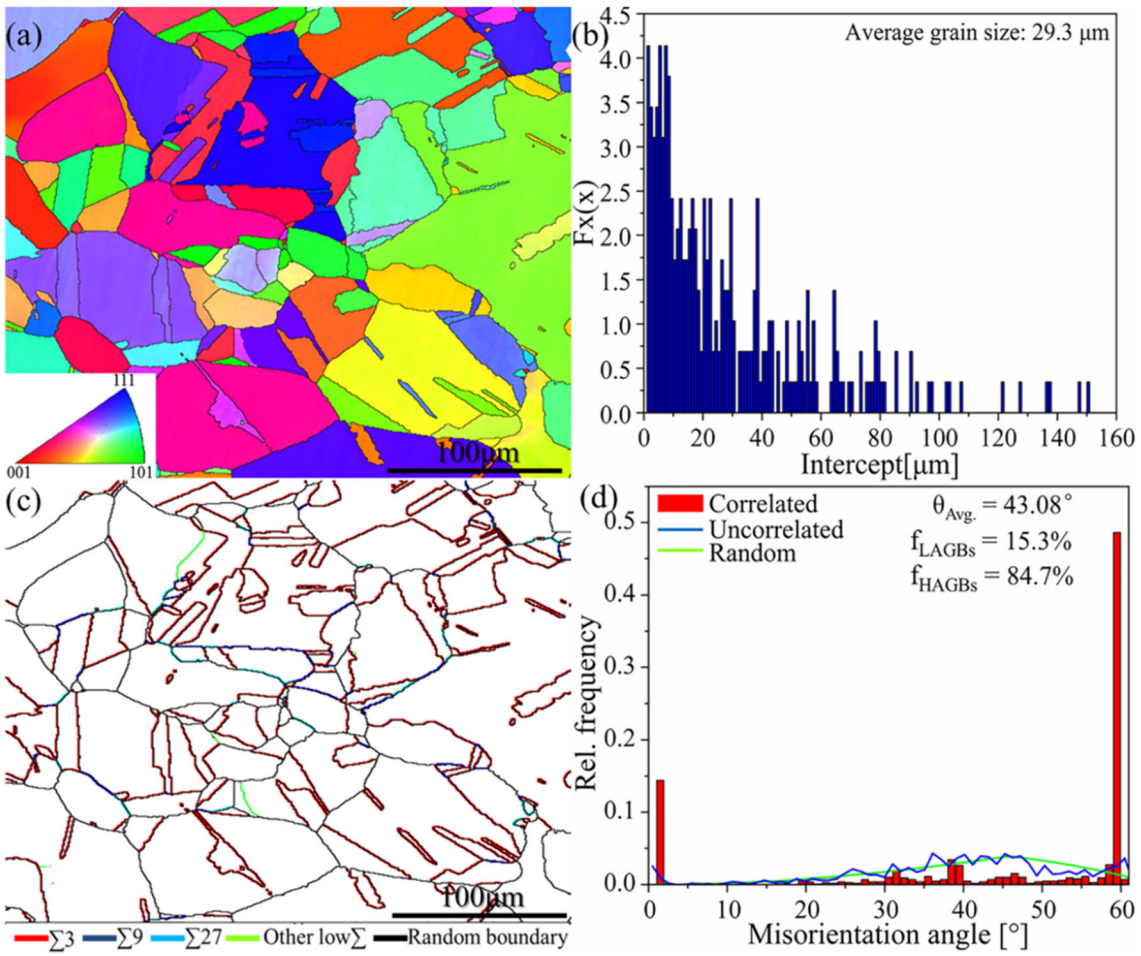

Fig. 1 Microstructure and grain boundaries of the as-annealed sheet: (a) inverse pole figure, (b) grain size distribution map, (c) CSL boundary map, and (d) misorientation angle distribution map

3.65%, respectively. And the average misorientation angle of annealed pure nickel N6 is 43.08°, which the high-angle grain boundaries is (HAGBs, $> 15°$) accounted for 84.7%.

Figure 2 displays the inverse pole figure maps (IPF maps) of pure nickel N6 with different degrees of cold rolling. Each grain is colored based on its crystal orientation, red is the [001] orientation, green is the [101] orientation, and blue is the [111] orientation. From Fig. 2, it is clear that the microstructural evolution is closely related to deformation. The microstructure of the sample after cold rolling to 20% of its initial thickness changes slightly, and equiaxed grains, thick laths, and twins could still be observed (Fig. 2a). With further straining, the grains are significantly refined and begin to gradually flatten and elongate in the direction of the main rolling strain (Fig. 2b). Further cold rolling to 70% of its thickness, the lath globalization process in the gauge part is well developed, grain shape aspect ratios are greatly increased, and many ultra-fine grains (UFGs) around the thin laths grain boundaries are observed (Fig. 2c). For the 90% cold-rolled sample, the grain boundaries are found to be broken and blurred, and smaller UFGs appear inside some grains. A quantitative description of the average grain diameters and average grain shape ratios is shown in Fig. 3. With increased cold rolling reduction, the average grain size decreases and the grain aspect ratio increases, which is consistent with that shown in Fig. 2.

Figure 4 shows the distribution of grain boundary misorientation angle and grain boundary maps of pure nickel N6 with various cold-rolled reductions. "Correlated" is misorientations calculated from neighboring points, "Uncorrelated" means misorientations calculated from random point in the scan, and "Random" shows the random distribution of misorientations for a purely random texture. From Fig. 4a, the grain boundary misorientation angle of the 20% cold-rolled sample shows a bimodal distribution and the fractions of low-angle grain boundaries (LAGBs, 2–15°) are relatively high, accounting for 68%. The average misorientation angle is 17.39°. From Figs. 4b–d, it can be observed that the LAGBs distribution of other

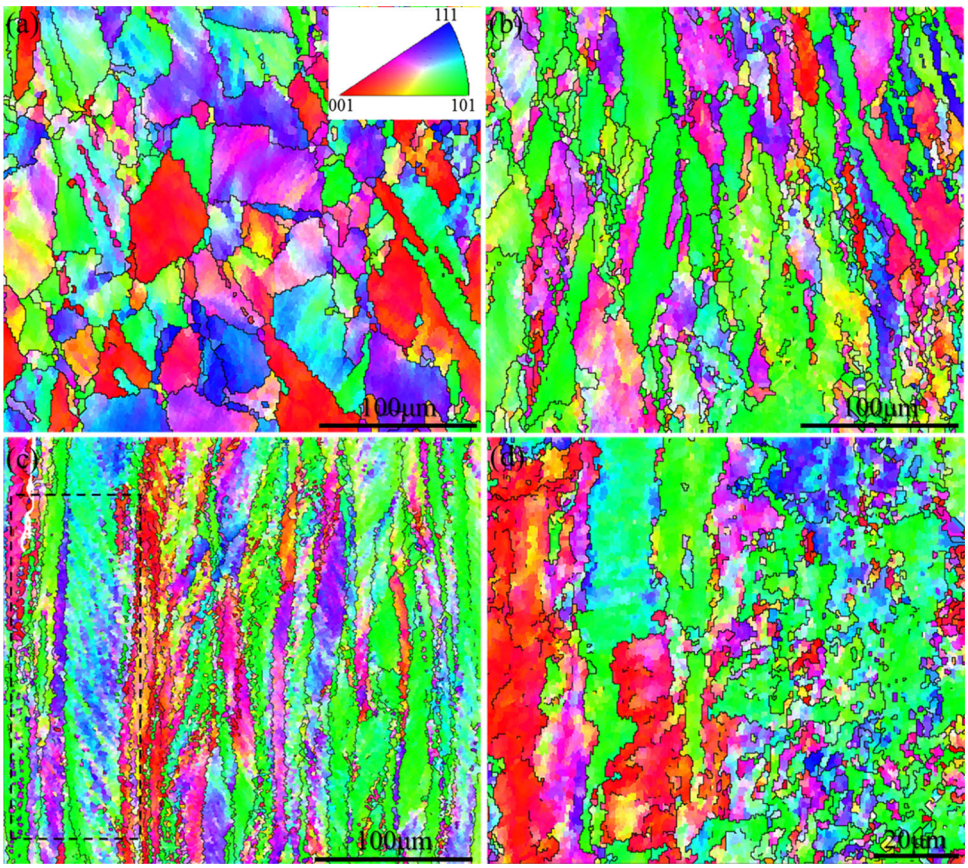

Fig. 2 EBSD inverse pole figure maps of pure nickel N6 with various CR reductions: (a) 20%, (b) 50%, (c) 70%, and (d) 90%

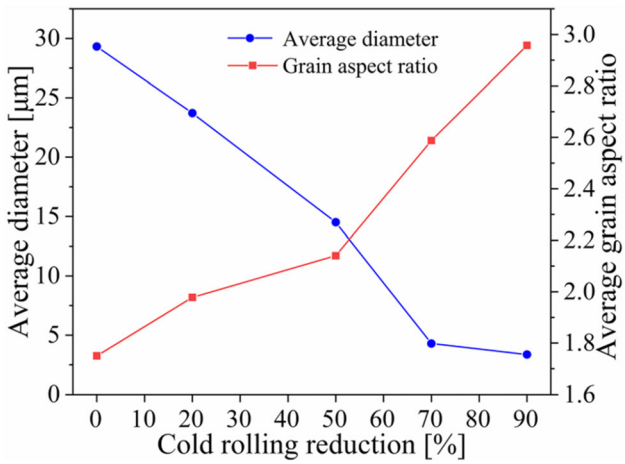

Fig. 3 Variation in average grain shape aspect ratio and average grain size of pure nickel N6 with various CR reductions

rolled samples are similar and the fractions of LAGBs increase with increasing cold rolling degree, and the average angles are 13.38°, 11.87°, and 10.43°, respectively. Furthermore, large deviations can be found between the uncorrected and random curves, which indicate that prominent rolling deformation textures are formed. In grain boundary mapping, the black line is HAGBs, the green is subgranular boundaries (SBs, $< 5°$), the red is $\Sigma 3$ boundaries, and the blue is other CSL boundaries. With increased cold rolling reduction, the grains elongate and deform along the rolling direction (RD) to form a lamellar structure. The lamellar structure is divided by HAGBs along the transverse direction (TD) of the samples. All grains with various cold-rolled reductions (Fig. 4) are filled with highly dense SBs to form large fractions of LAGBs, which result from the rearrangement and movement of accumulated dislocations. At the same time, the fraction of $\Sigma 3$ and other CSL boundaries drastically decrease (Fig. 5).

3.2 Textural Evolution

To better distinguish and understand the most important textural components of fcc metals located in $\varphi 2 = 0°$, 45°, and 65° sections of Euler angle spaces, their positions are schematically indicated in Fig. 6. The ODFs of pure nickel N6 in annealed and other cold-rolled reductions are represented in these Euler angle space sections, which are calculated and depicted in Fig. 7. It is found that the annealed material is characterized by a Brass$\{011\} < 211 >$ component, S$\{123\} < 634 >$ component, and rather random and slightly annealed texture dominated by the Cube$\{001\} < 001 >$ component

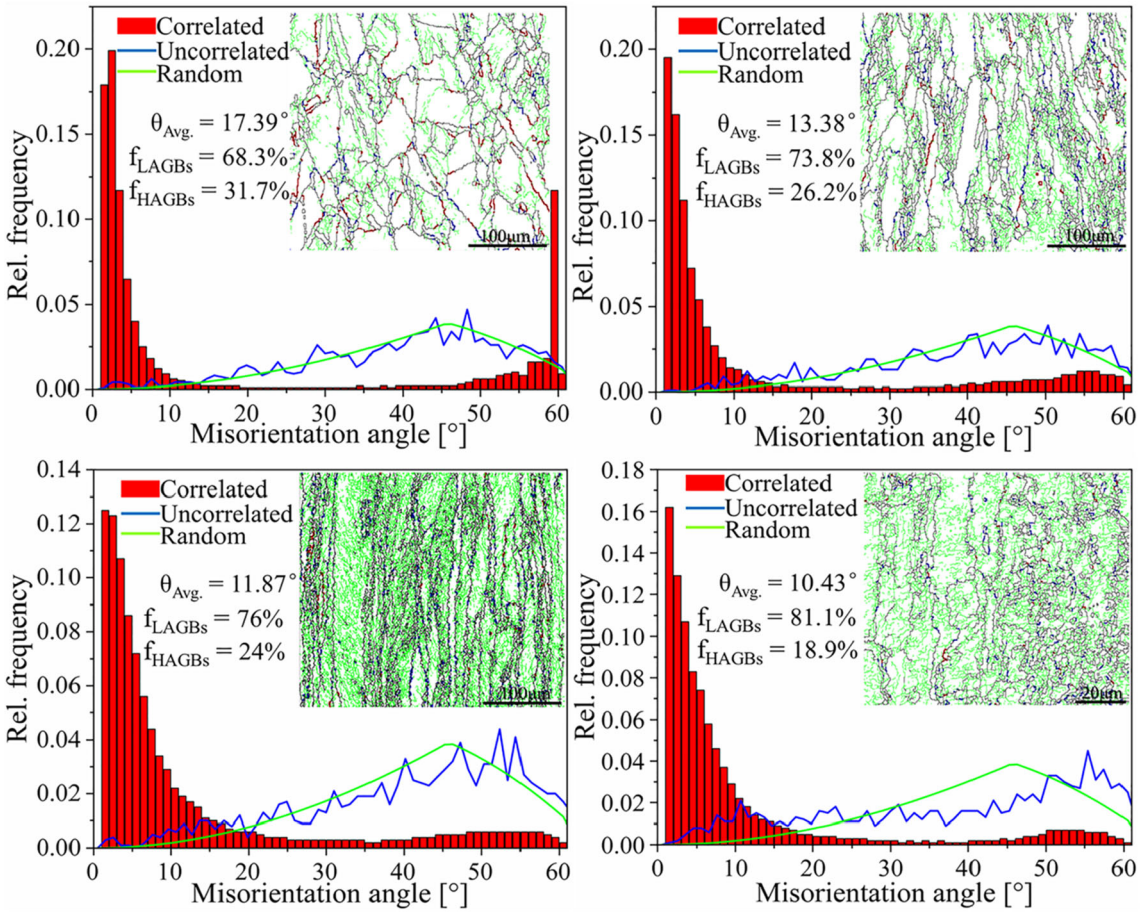

Fig. 4 Misorientation angle distributions of N6 at different CR reductions (the inset shows the EBSD grain boundary maps): (a) 20%, (b) 50%, (c) 70%, and (d) 90%

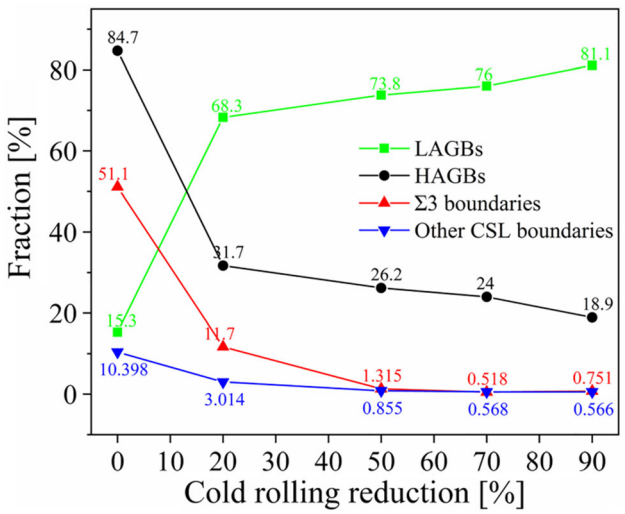

Fig. 5 Variation in the fraction of grain boundaries and CSL boundaries of pure nickel N6 with various CR reductions

(Fig. 7a). It is generally believed that medium-to-low stacking fault energy (SFE) metals are likely to form a Brass-type texture [18]. The 20% cold-rolled thickness reduction (Fig. 7b) of pure nickel N6 results in the development of a deformation texture that is mainly composed of Goss$\{011\} < 001 >$, Rotated Goss$\{110\} < 110 >$, P$\{011\} < 112 >$, and Brass$\{011\} < 211 >$ orientations. Further cold rolling to 50%, three texture components (Brass, Rotated Goss, and P) remain and their intensities decrease. At the same time, the obtained crystallographic textures also are shear textures, which are dominated by shear 3$\{111\} < 110 >$ and Shear 4$\{112\} < 110 >$, which are strictly related to the imposed shear strain[21, 22]. Previous studies believe that rolling rolls must rely on surface friction to bring the sheets into the roll gap to achieve rolling deformation. When this friction force is high enough and induces significant additional shear strain, it will promote the formation of shear texture on the sheet surfaces [15, 23]. With increase in the cold-rolled reduction up to 70%, the Brass and P texture components almost disappear and new texture types dominated by shear 2 $\{111\} < 112 >$ and Cu $\{112\} < 111 >$ components form. For the 90% cold-rolled sample, the texture composition is mainly shear 4. At the same time, the cube texture is reformed. Previous studies indicated that the texture mainly

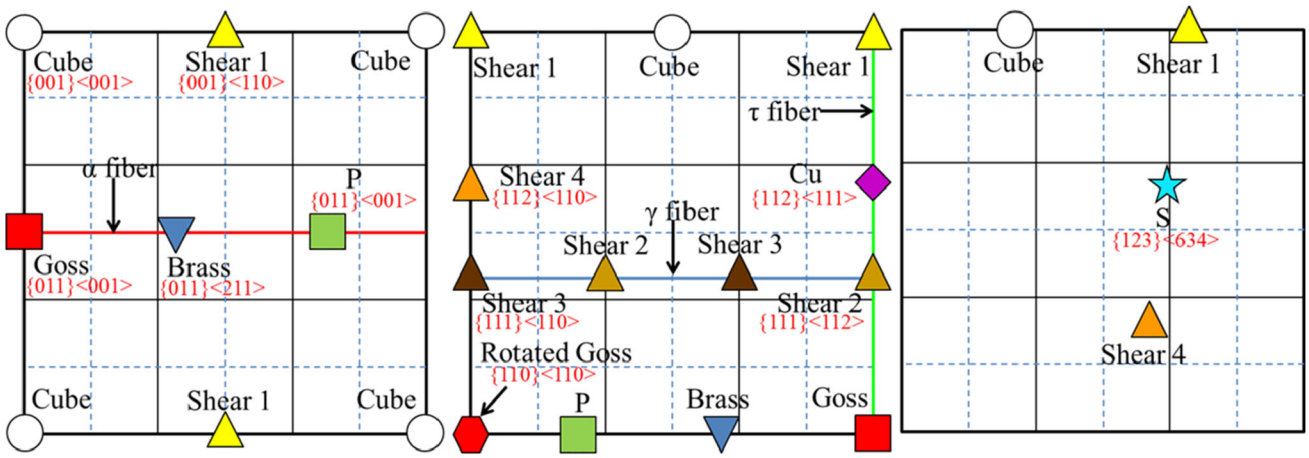

Fig. 6 Nominal position of basic texture components

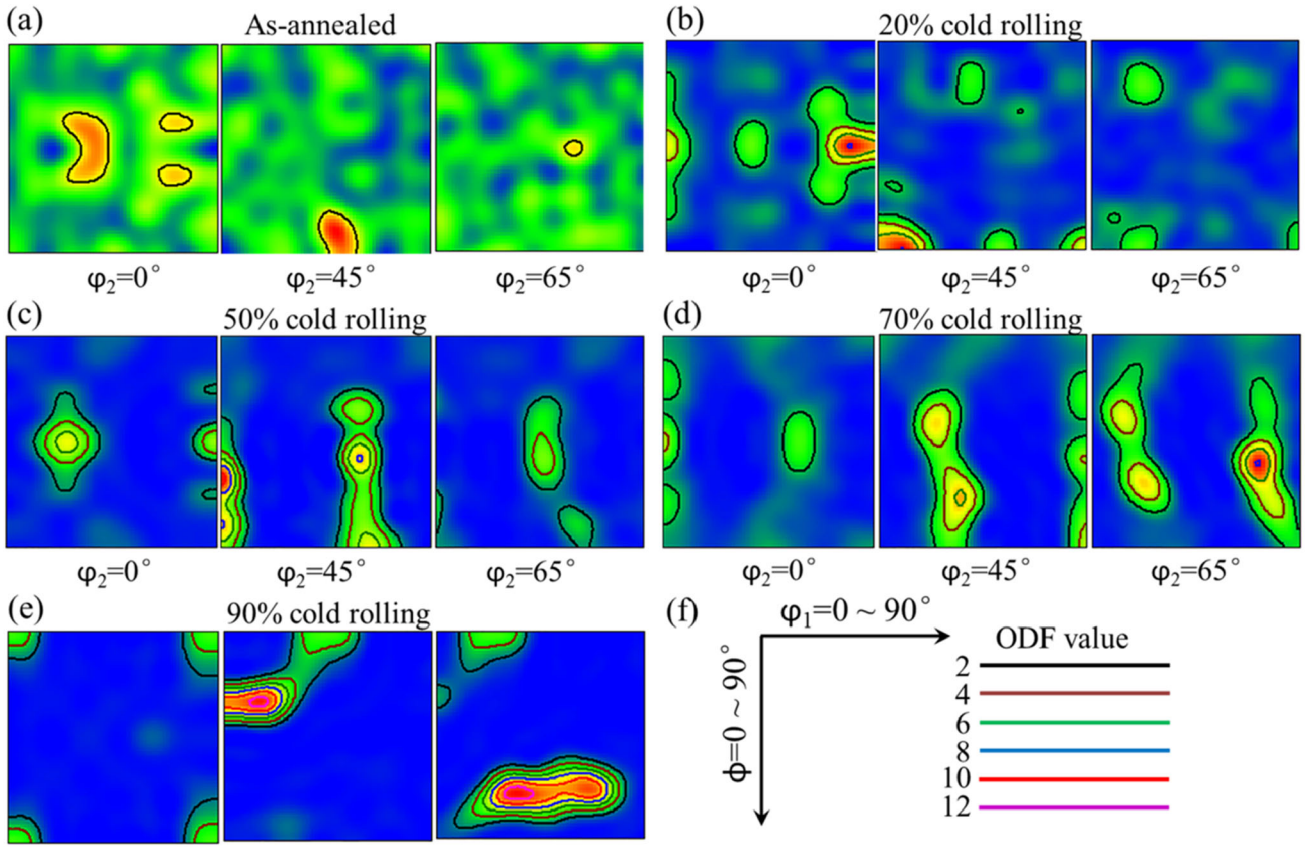

Fig. 7 Crystallographic texture development represented in φ 2 = 0°, 45°, and 65° of the Euler space: (a) as-annealed, (b) 20%, (c) 50%, (d) 70%, and (e) 90%

includes S, Brass (Bs), and Copper 3 orientations in highly rolled pure nickel [24, 25]. But in this study, the texture mainly is shear orientation when cold-rolled thickness reduction exceeds 50%. The reason for this result is that the single-pass with the large-deformation rolling method used in this study, which is different from the multi-pass small deformation method used in the previous study.

Figure 8 shows the α-fiber, γ-fiber, and τ-fiber plot calculated for the as-annealed and cold-rolled N6 at different CR reductions. The changes in ODF values reveal that the Brass $\{011\} < 211 >$ component (lying along the α-fiber, Fig. 8a) generally shows higher intensity than that of Copper $\{112\} < 111 >$ (τ-fiber, Fig. 8c) except for the 70% cold rolling reduction condition. When the cold

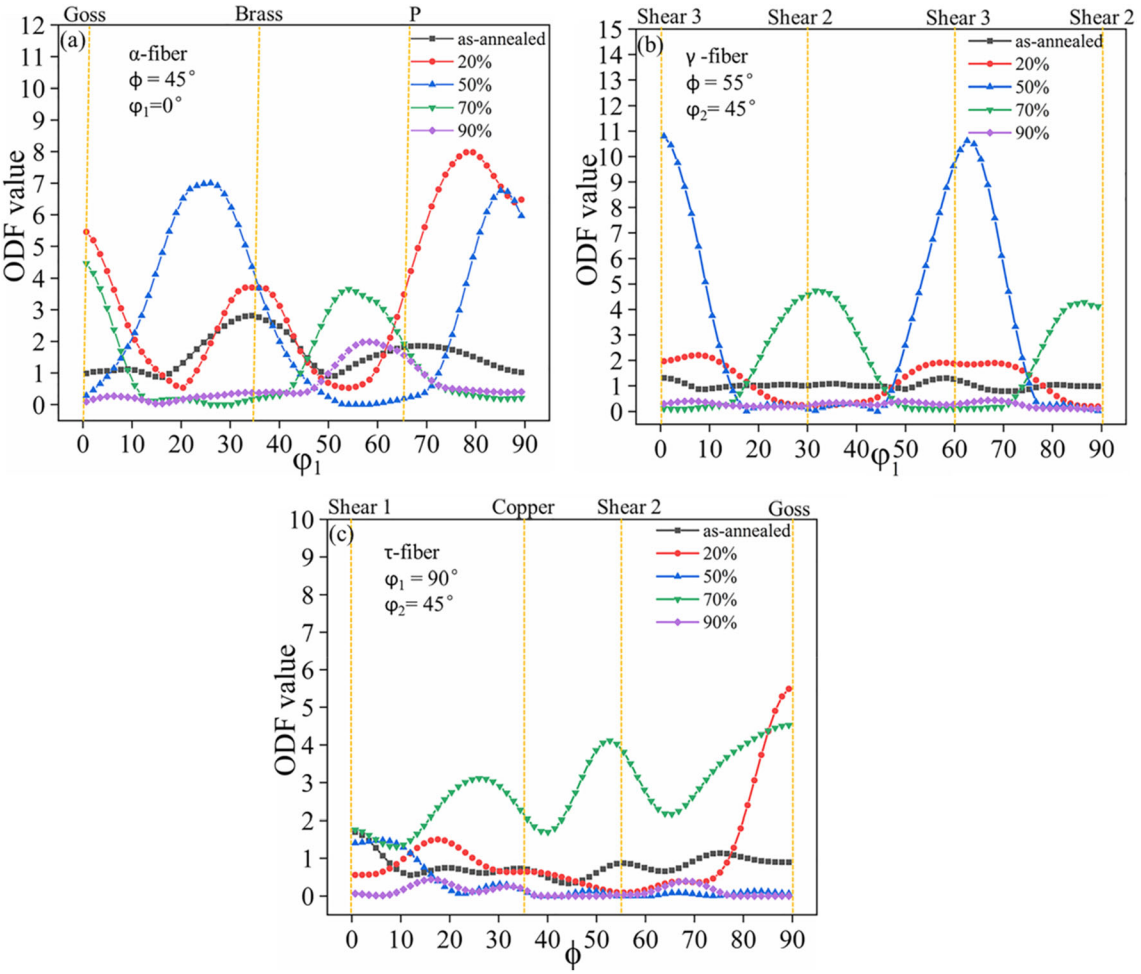

Fig. 8 Changes in ODF values along α-fiber (a), γ-fiber (b), τ-fiber (c) calculated for pure nickel N6 in annealed condition and after various cold-rolled reduction thicknesses

rolling reduction is less than 50%, the ODF value of the shear texture (shear 1, shear 2, shear 3, and shear 4) is very small. However, in the case of 50% cold rolling degree, the ODF value of the shear 3 texture reaches 11, which is much higher than the ODF value of all other textures. According to the ODFs in Figs. 7 and 8, when rolling degree is 50%, shear textures appear, which are dominated by Shear $3\{111\} < 110 >$. And the maxima of Shear $3\{111\} < 110 >$ intensity reaches 11. Further cold rolling to 70%, shear texture is still the main texture, but changes from shear $3\{111\} < 110 >$ to Shear 2 $\{111\} < 112 >$. When cold rolled to 90%, the texture composition is mainly shear 4 $\{112\} < 110 >$ and its intensity exceeds 12, which is higher than all shear texture types.

3.3 Grain Orientation

Further exploration of the misorientation gradient of the dominant orientation grains during CR process, the point-to-point, and point-to-origin misorientations of as-annealed sample and cold-rolled sample with 70% reduction thickness are quantified and depicted in Figs. 9 and 10, respectively. Figure 9a shows the main texture of the as-annealed specimen, and Figs. 9b–e show the point-to-point and point-to-origin misorientations along the arrows (P1, P2, P3,and P4) in Fig. 9a for different textures. Red represents point-to-origin source misorientation, and blue represents point-to-point misorientation. The point-to-point misorientation values for different textures show a typically fluctuating lattice orientation and the peaks do not exceed 1°. The point-to-origin profiles for different textures display no accumulative trend and the misorientations do not typically reach 2°, which shows the random orientation characteristics of the dislocation-free grains [24]. The local misorientation gradient is quite weak within the different textures of the as-annealed sample, which is because the material undergoes substructure transformation and dislocation rearrangement to prevent the formation of high

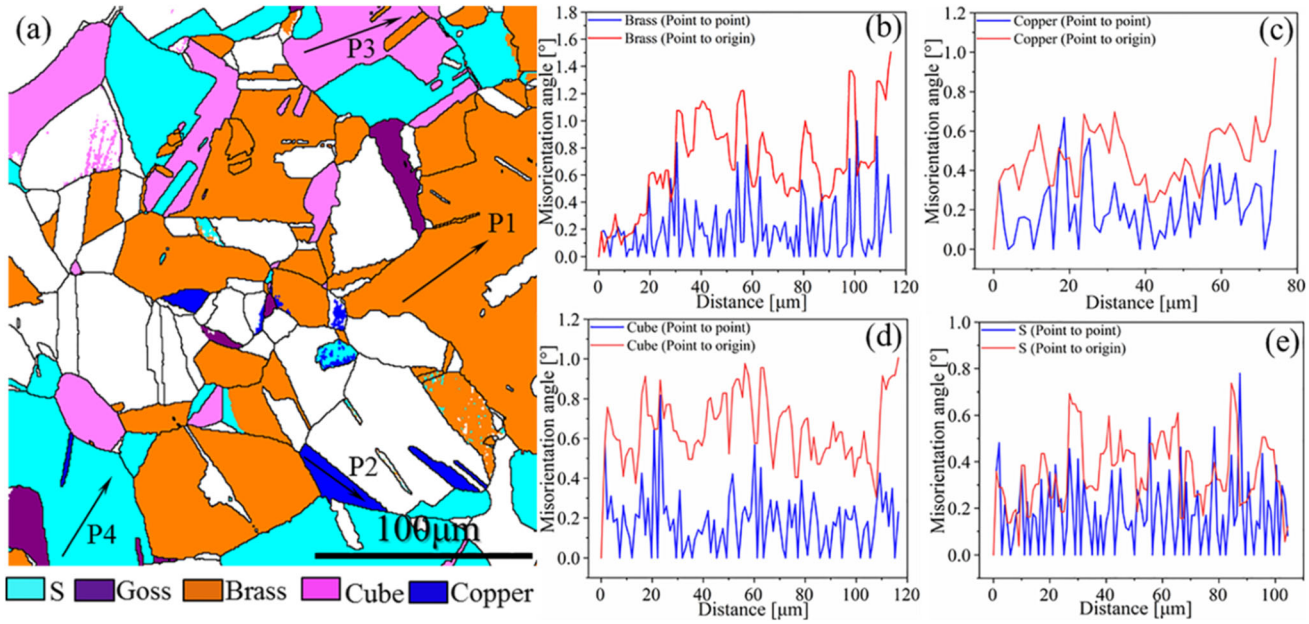

Fig. 9 Misorientation gradient scans along the lines in the dominant texture components: (a) texture distribution map in as-annealed condition; (b)–(e) misorientation gradients

intragranular local dislocation gradients during the annealing process [25].

A subset of Fig. 2c (marked by the rectangle) through EBSD analysis was made to explore the misorientation gradient developed in the cold-rolled sample with 70% thickness reduction, as shown in Fig. 10. Figure 10a illustrates that the deformed sample consists of different textures, and these orientation textures are separated by HAGBs and are distributed unevenly. A line scan corresponding to the black arrow is conducted within the different textures of deformed grains and the measured misorientation profile is depicted in Figs. 9b–f. The point-to-origin profile accumulates misorientations constantly, showing the high misorientation gradient (exceeding 10°). It clearly indicates dislocation multiplication within deformed grain due to cold rolling. Furthermore, the grain orientation in shear textures (shear 2 and shear 4) presents a higher misorientation gradient (exceeding 20°), which is related to the shear strain caused by friction. A unidirectional shear stress always exists on the surface of the rolled sheet during the large cold-rolled reduction thickness, which induces an obvious rotation of the rolling stress tensor around the transverse direction in the surface layer and stronger intergranular mechanical interactions [26].

4 Discussion

In the normal rolling process, the material in the rolling seam mainly bears three-dimensional compressive stress. After removing the hydrostatic stress that has no effect on plastic deformation, the principal stress state of the material can be simplified as $\begin{bmatrix} \sigma_1 & 0 & 0 \\ 0 & 0 & 0 \\ 0 & 0 & \sigma_3 \end{bmatrix}$

Among them, $\sigma_1 > 0$ is the rolling tensile stress, and $\sigma_3 < 0$ is the normal compressive stress of the plate. In the process of rolling deformation with large reduction, the roll relies on the surface shear stress τ to bring the rolled sheet into the roll gap. This shear stress will cause the corresponding shear stress σ_{31} inside the rolled sheet (Fig. 11b) and transforms the principal stress value into $\sigma'_1 < 0$ and $\sigma'_3 < 0$, which enables the principal stress state in the rolled plate to laterally rotate.

Figure 12 shows the Schmid factor distributions of crystals in the cold-rolled sample with 90% reduction under different slip systems. Different colors represent different deform abilities of the crystals. When the Schmid factor changes from 0 to 0.5 (color changes from blue to red correspondingly), the crystal changes from hard orientation to soft orientation [27]. The closer the Schmidt factor is to 0.5, the easier the grains will slip. From Fig. 10c, it can be seen that the proportion of Schmidt factor in the 0.48–0.5 interval is about 30% in the slip system $\{112\} < 110 >$, which is much larger than that of the $\{111\} < 110 >$ slip system (accounting for 16%). This

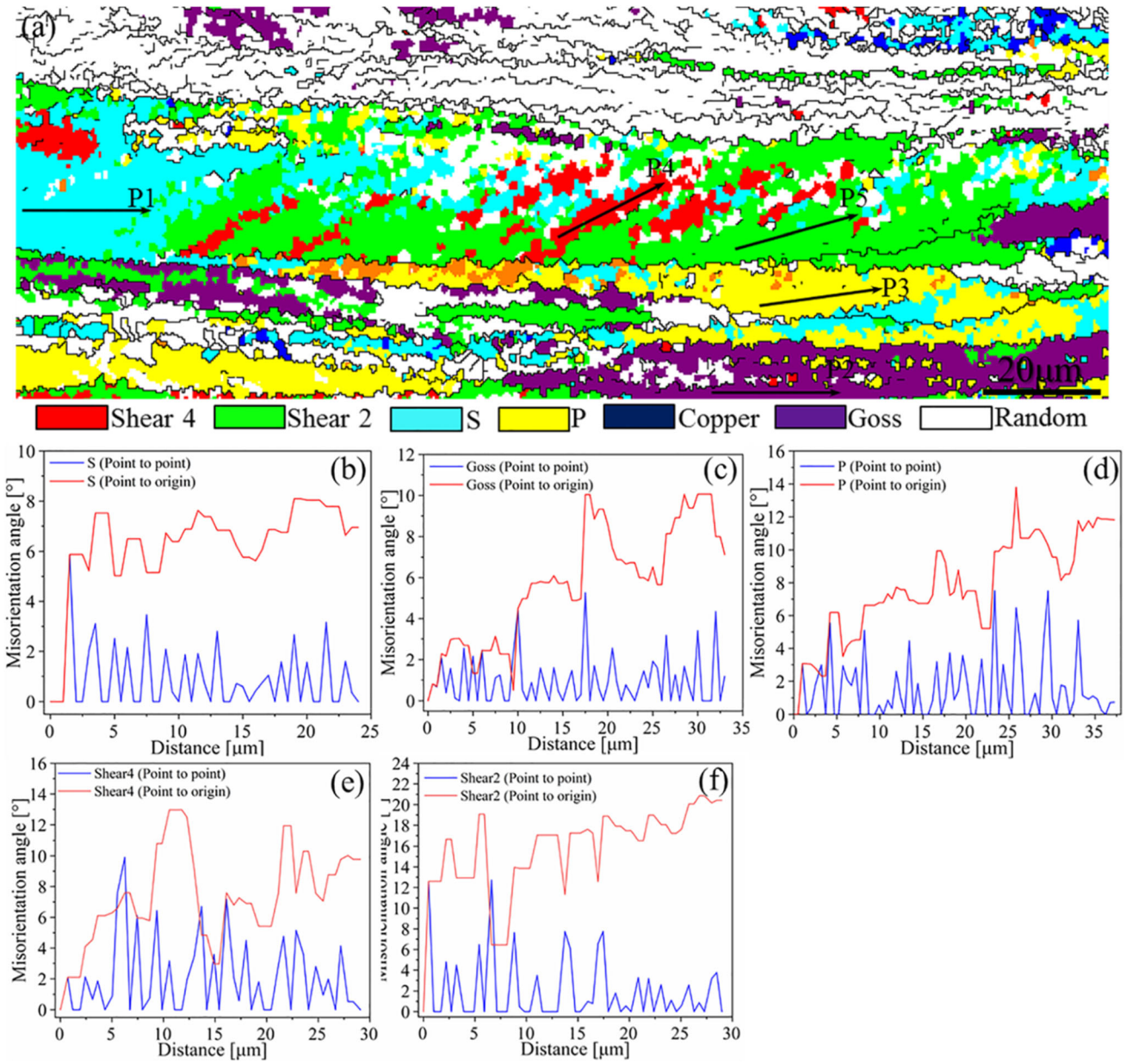

Fig. 10 Misorientation gradient scans along the lines in the dominant texture components: (a) texture distribution map in 70% cold-rolled thickness reduction; (b)–(f) misorientation gradients

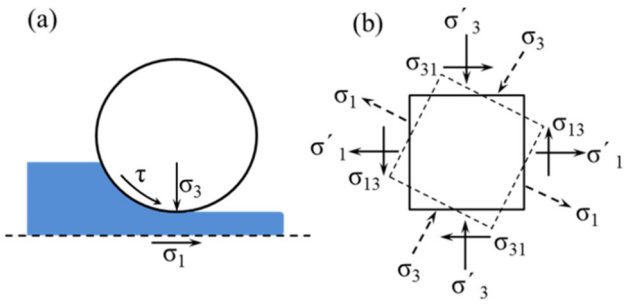

Fig. 11 (a) Schematic diagram of plate stress during cold rolling and (b) stress state

implies that the crystals can more easily slip along the $\{112\} < 110 >$ slip system. The strong shear stress on the surface of the rolled plate changes the stress state, the active slip system is also adjusted accordingly, which will significantly change the deformation behavior of the grains [28]. Therefore, this change causes the normal cold-rolled texture dominated by $Cu\{112\} < 111 >$, $S\{123\} < 634 >$, $Brass\{011\} < 211 >$ and other stable orientation grains to rotate around the transverse direction to a shear texture composed of $Shear4\{112\} < 110 >$ and $\{110\}\|RD$ fiber textures.

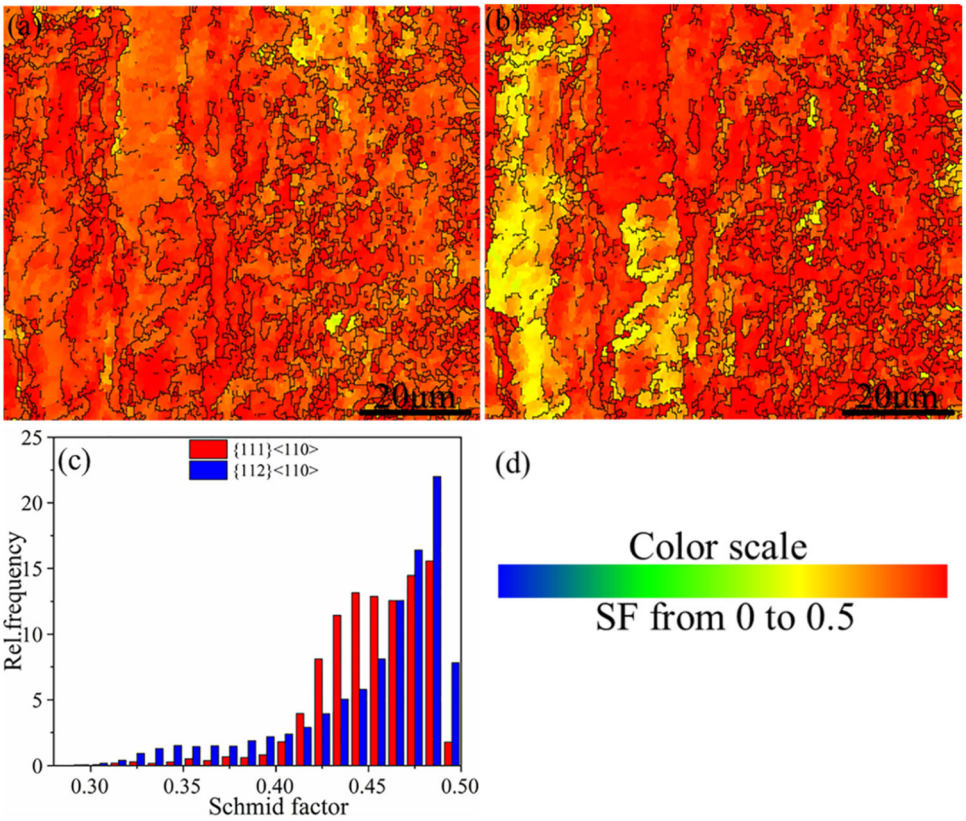

Fig. 12 Crystal deform ability of the cold-rolled sample with 90% thickness reduction under $\{111\} < 110 >$ and $\{112\} < 110 >$ slip system: (a) Schmid factor map under $\{111\} < 110 >$, (b) Schmid factor map under $\{112\} < 110 >$, (c) Schmid factor distribution chart, and (d) scale bar

5 Conclusions

In this study, a single-pass large-deformation rolling method was used to study the microstructure and textural characteristics of pure nickel N6 caused by the variation of cold rolling degree. The major findings drawn from this work are summarized in the following:

(1) With the increase of cold rolling reduction, the microstructure evolves from micro-bands (MB) to lamellar-bands (LB). In the high-deformation base-band, the LB structure is almost parallel to the RD direction. At the same time, the inside of the LB structure is filled with a mass of SBs.

(2) When cold rolling reduction exceedes 50%, shear textures gradually become the main texture component and other textural intensities decrease in cold-rolled samples. And the shear texture component changes from shear $3\{111\} < 110 >$ to Shear $2\{111\} < 112 >$, and finally to shear $4\{112\} < 110 >$ as the amount of cold rolling reduction increases.

(3) The strong shear stress on the surface of the rolled plate changes the stress state, also changes the deformation behavior of the grains, which causes the normal cold-rolled texture dominated by $Cu\{112\} < 111 >$, $S\{123\} < 634 >$, Brass$\{011\} < 211 >$ to rotate around the transverse direction to form a shear texture composed of Shear4$\{112\} < 110 >$ and $\{110\}\|RD$ fiber textures.

Acknowledgements Zhi Jia would like to gratefully acknowledge the support of the National Nature Science Foundation of China (No. 51665032), Science Foundation for Distinguished Young Scholars of Gansu Province (18JR3RA134), and Nation Natural Science Foundation of China [No.51664041].

References

[1] Z.X. Gao, Z. Jia, J.J. Ji, D.X. Liu, and Y.T. Ding, *Phy. Eng. Metall. Mater: CMC 2018* **217** (2019) 201.
[2] G. R. Thellaputta, P. S. Chandra, and C.S.P. Rao, *Mater Today Proc* **4** (2017) 3712.
[3] G. Palumboa, F. Gonzaleza, A.M. Brennenstuhl, U. Erb, W. Shmayda, and P.C. Lichtenberger, *Nanostruct Mater* **9** (1997) 737.
[4] B.M. Guyot, N.L. Richards, and *Mater Sci Eng A* **395** (2005) 87.
[5] W. Polkowski, A. Polkowska, and D. Zasada, *Mater Charact* **130** (2017) 173.
[6] K. Wang, N.R. Tao, G. Liu, J. Lu, and K. Lu, *Acta Mater* **54** (2006) 5281.
[7] D.A. Hughes, N. Hansen, *Acta Mater* **48** (2000) 2985.
[8] Z.P. Luo, H.W. Zhang, N. Hansen, and K. Lu, *Acta Mater* **60** (2012) 1322.
[9] X.C. Liu, H.W. Zhang, and K. Lu, *Acta Mater* **96** (2015) 24.
[10] C. Chen, S. Wang, Y.L. Jia, M.P. Wang, Z. Li, and Z.X. Wang, *Mater Sci Eng A* **601** (2014) 131.

[11] P. Hu, F. Yang, K.S. Wang, Z.T. Yu, J.F. Tan, R. Song, B.L. Hu, H.W., H.C. He, and A.A. Volinsky, *Int J Refract Met Hard Mater* **32** (2015) 131.
[12] P. Hu, Y.H. Zhou, T. Chang, Z.T. Yu, K.S. Wang, F. Yang, B.L. Hu, W.C. Cao, and H.L. Yu, *Mater Sci Eng A* **687** (2017) 276.
[13] T. Leffers, R.K. Ray, *Prog Mater Sci* **54** (2009) 351.
[14] X.P. Chen, X. Chen, J.P. Zhang, and Q. Liu, *Mater Sci Eng A* **585** (2013) 66.
[15] N.P. Gurao, S. Sethuraman, and S. Suwas, *Mater Sci Eng A* **528** (2011) 7739
[16] J.N. Qin, D. Zhang, G.D. Zhang, and J.C. Lee, *Mater Sci Eng A* **408** (2005) 79.
[17] H. Akhiani, M. Nezakat, and J.A. Szpunar, *Mater Sci Eng A* **614** (2014) 250.
[18] A. Polkowska, S. Lech, and W. Polkowski, *Mater Sci Eng A* **787** (2020) 139478.
[19] X.L. Li, W. Liu, A. Godfrey, D.J. Jensen, Q. Liu, *Acta Mater* **55** (2007) 3531.
[20] B.M. Guyot, N.L. Richards, *Mater Sci Eng A* **395** (2005) 87.
[21] B. Verlinden, J. Driver, I. Samajdar, R.D. Doherty, and R.W. Cahn, *Thermo- Mechanical Processing of Metallic Materials*, Elsevier, Oxford (2007).
[22] W. Truszkowski, J. Krol, and B. Major, *Met Trans* **11A** (1980) 749.
[23] C.H. Choi , J.W. Kwon, E.H. Oh, *Acta Mater*. 1997, 45(21), 5119.
[24] L.X. Wang, X.P. Chen, W. Xie, P. Ren, and L. Mei, *Rare Metal Mat Eng* **48** (2019) 3022.
[25] M.J. Wang, C.Y. Sun, M.W. Fu, Z.L. Liu, and C.H. Wang, *Mater Design* **188** (2019) 108429.
[26] Y.C. Lin, X.Y. Wu, X.M. Chen, J. Chen, D.X. Wen, J.L. Zhang, and L.T. Li, *J Alloys Compd* **640** (2015) 101.
[27] Z. Jia, Z.X. Gao, and J.J Ji, *Adv Eng Mater* **22** (2020) 1901445.
[28] Y.M. , H.P. Ren, and W.M. Mao, *Journal of Inner Mongolia University of Science and Technology* **38** (2019) 331.